

# Disentangling the Ultrafast Nonlinear Optical Behavior of Plasmonic Resonances Near the Interband Transition

Andrea Schirato, Mychel G. Silva, Danielle C. Teles-Ferreira, Cristian Manzoni, Ana Maria de Paula, Giulio Cerullo,\* Giuseppe Della Valle,\* and Marcel Di Vece\*

The photoexcitation of plasmonic nanostructures with ultrashort laser pulses allows for elucidating the mechanisms underlying the ultrafast nonlinear optical response of such systems, gaining insight into the fundamental processes triggered by light absorption at the nanoscale. To date, the complex temporal and spectral features of the photoinduced response are not fully understood, especially when the photon energies are close to the interband transitions of the metallic medium. Herein, the effects of photoexcitation of plasmonic nanostructures are studied by resorting to a combination of broadband transient absorption spectroscopy and semiclassical nonlinear simulations of the energy relaxation processes following illumination. The proposed approach enables an in-depth disentanglement of all the contributions to the ultrafast transient optical response of supported gold nanocrystals. From these methods, the apparent transient blue shift of the localized plasmon resonance observed in the pump-probe signals is rationalized as an interplay between different and spectrally dispersed permittivity modulations, instead of a simple negative permittivity change, as it could be concluded based on the Fröhlich condition. The results provide a comprehensive understanding of the thermo-modulational nonlinearities of plasmonic nanostructures exhibiting resonances close to the interband transition threshold.

of the interband transitions and subsequent variation of noble metal permittivity at the nanoscale. In turn, transient modifications (typically on the picosecond time-scale) of the material permittivity result in a high-speed all-optical modulation of the resonant extinction cross-section of the nanostructure, a unique feature lying indeed at the heart of ultrafast plasmonics.<sup>[7–11]</sup> The quantitative description of the transient optical response of the nanostructure due to photoinduced permittivity changes has been the subject of numerous studies and multiple approaches have been reported, at different levels of complexity, from ab initio atomistic calculations<sup>[12,13]</sup> to reduced models at the quantum<sup>[14]</sup> or even semiclassical level.<sup>[3,6,15,16]</sup> In all the proposed approaches, the optical nonlinearities dictating the system behavior are complex-valued, namely consisting of photoinduced modulation processes of both the real and the imaginary part of the metal permittivity  $\epsilon_m$ , producing changes in the optical properties which are highly dispersed in frequency across the visible spectral region.<sup>[6,12,16]</sup>


## 1. Introduction

Noble-metal plasmonic nanostructures are well known to exhibit a giant delayed thermo-optical nonlinearity, governed by the dynamics of photoexcited hot electrons.<sup>[1–6]</sup> Specifically, out-of-equilibrium carriers are responsible for an ultrafast modulation

As a result of such complexity in the light-driven modification of the metal properties, the phenomenology of all-optical modulation of the nanostructure response is rather rich. For instance, it has been shown<sup>[17]</sup> that the surface plasmon polariton (SPP) resonance in metallic films excited with ultrashort laser pulses exhibits a transient spectral shift which could correspond to

A. Schirato, G. Cerullo, G. Della Valle  
Dipartimento di Fisica  
Politecnico di Milano  
Piazza Leonardo da Vinci 32, I-20133 Milano, Italy  
E-mail: giulio.cerullo@polimi.it; giuseppe.dellavalle@polimi.it

A. Schirato  
Istituto Italiano di Tecnologia  
via Morego 30, I-16163 Genova, Italy

 The ORCID identification number(s) for the author(s) of this article can be found under <https://doi.org/10.1002/adpr.202200081>.

© 2022 The Authors. Advanced Photonics Research published by Wiley-VCH GmbH. This is an open access article under the terms of the Creative Commons Attribution License, which permits use, distribution and reproduction in any medium, provided the original work is properly cited.

DOI: 10.1002/adpr.202200081

M. G. Silva, A. M. de Paula  
Departamento de Física  
Universidade Federal de Minas Gerais  
Belo Horizonte, MG 31270-901, Brazil

D. C. Teles-Ferreira  
Instituto Federal de Minas Gerais  
Campus Ouro Preto, Ouro Preto, MG 35400-000, Brazil

C. Manzoni, G. Cerullo, G. Della Valle  
Istituto di Fotonica e Nanotecnologie  
Consiglio Nazionale delle Ricerche  
Piazza Leonardo da Vinci 32, I-20133 Milano, Italy

M. Di Vece  
CIMAINA and Dipartimento di Fisica  
Università degli studi di Milano  
Via Celoria 16, 20133 Milano, Italy  
E-mail: marcel.divece@unimi.it

either a blue or a red shift. The character of the shift depends on the spectral position of the SPP in static (unperturbed) conditions, which can be either below or above the specific wavelength at which the real part of the metal permittivity modulation,  $\Delta\epsilon'_m$ , changes its sign from negative to positive. For gold, this threshold wavelength resides around 550 nm, i.e., close to the edge of interband transitions, starting at around 510 nm.

Following results on thin films, the transient plasmonic spectra of noble metal nanoparticles have been interpreted according to the same reasoning, as illustrated in **Figure 1** for the simple case of a spherical nanoparticle. For such a nanostructure, the localized surface plasmon resonance (LSP) occurs at a wavelength  $\lambda_R$  defined by the Fröhlich condition:  $\epsilon'_m(\lambda_R) + 2\epsilon_d = 0$ , which is valid for nanospheres much smaller than the optical wavelength,<sup>[18]</sup> where  $\epsilon_m = \epsilon'_m + i\epsilon''_m$  and  $\epsilon_d$  are the permittivities of the metal and of the dielectric environment, respectively (see inset in Figure 1a).

Because of the typical spectral shape of  $\epsilon'_m(\lambda)$  in noble metals (black curve in Figure 1a), a positive permittivity variation  $\Delta\epsilon'_m$  (red curves in Figure 1a, of increasing amplitude from dotted, dash-dotted to solid lines) induces a spectral shift of  $\lambda_R$  toward longer wavelengths (Figure 1c, top panel). Therefore, when the LSP is located at longer wavelengths compared to the metal interband transitions (i.e., when it falls in the spectral region corresponding to a photoinduced  $\Delta\epsilon'_m > 0$ ), ultrafast transient extinction spectra ( $\Delta\sigma_E/\sigma_E$ ) with a characteristic derivative shape are observed, arising from the red shift of the LSP, which we will refer to as positive derivative shape (Figure 1c, middle panel). In fact, such interpretation was reported for the first time in a seminal article on silver nanoparticles,<sup>[15]</sup> and represents now a well-established view within the ultrafast plasmonics community. On the contrary, a negative variation of the metal permittivity  $\Delta\epsilon'_m$  (blue curves in Figure 1a, larger in modulus from dashed, dash-dotted to solid curves) determines, according to the Fröhlich condition, a shift of  $\lambda_R$  toward shorter wavelengths (Figure 1b, top panel). As a consequence, a LSP sitting at shorter wavelengths compared to the interband edge of the metal (where the photoinduced  $\Delta\epsilon'_m < 0$ ) experiences a blue shift, resulting thus in a characteristic transient spectrum of an opposite sign with respect to the previous case, which we will refer to as a negative derivative shape (Figure 1b, middle panel). This effect is consistent with the results reported by several groups and for different plasmonic structures, e.g., for Au nanospheres<sup>[13]</sup> and nanorods (when considering their transverse LSP).<sup>[3,19]</sup> Note that according to this picture, larger permittivity modulations (in modulus) due to increasing level of photoexcitation (e.g., because of higher pump fluence) give rise to larger spectral (either red or blue) shifts, as well as to increasing amplitudes of the derivative transient signal (cfr. dotted, dash-dotted, and solid curves in Figure 1b,c, with the same meaning of the line style as in Figure 1a). Finally, it is worth noting that, in a typical pump-probe experiment, the ultrafast transient spectra are measured in terms of the relative differential transmission of the sample  $\Delta T/T \propto -\Delta\sigma_E/\sigma_E$ , as sketched in Figure 1b,c, bottom panels.

Although this interpretation of the photoexcited spectra in plasmonic nanostructures is well accepted, there are still key

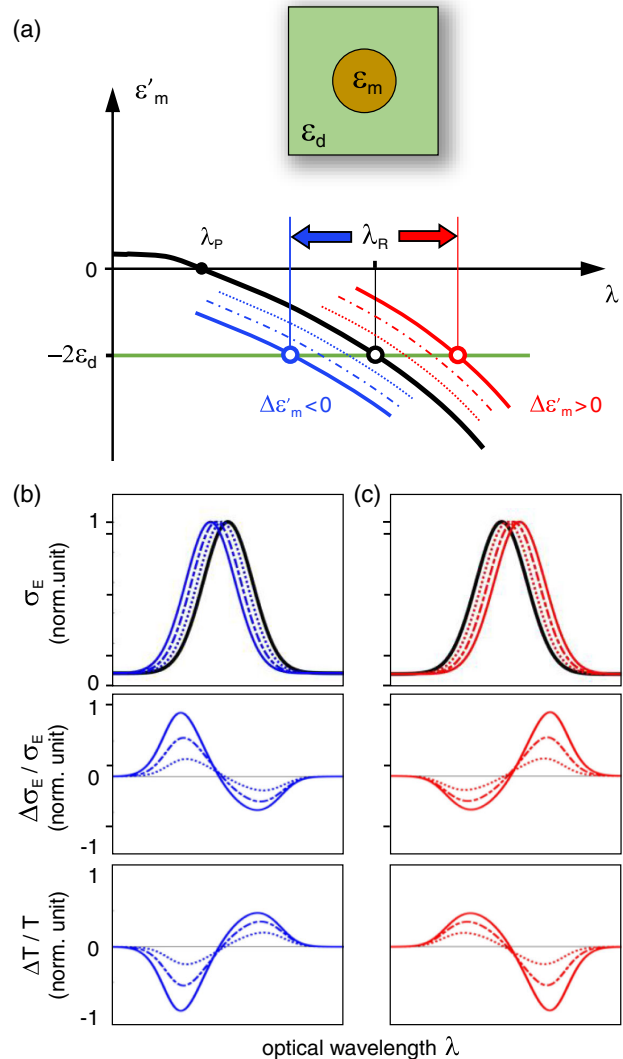


**Figure 1.** a) Sketch of the photoinduced spectral shift for the localized plasmon resonance of a metallic nanosphere (inset). The plasmonic resonance wavelength  $\lambda_R$  is determined by the Fröhlich condition for a given modulation of the metal permittivity real part,  $\Delta\epsilon'_m$ ; the zero-crossing wavelength  $\lambda_p$  identifies the wavelength corresponding to the plasma frequency. A positive  $\Delta\epsilon'_m$  results in an increase of metal permittivity (red curves, mimicking a larger modulation from dotted, dash-dotted to solid lines) with respect to its equilibrium value (black curve), whereas a negative  $\Delta\epsilon'_m$  (blue curves, larger in modulus from dashed, dash-dotted to solid lines) entails a decreased permittivity. b,c) Sketch of the corresponding spectral (either blue or red) shift of the extinction cross-section  $\sigma_E(\lambda)$  (top panels) for increasing values of the  $|\Delta\epsilon'_m|$ , of the resulting transient spectra of the relative differential extinction  $\Delta\sigma_E/\sigma_E$  (middle panels) exhibiting a (either negative or positive) derivative shape, and of the relative differential transmission  $\Delta T/T$  spectra (bottom panels) that can be measured in a pump-probe experiment. The static (black) and transient (blue or red) extinction cross-section spectra are mimicked with Gaussian profiles of fixed width and amplitude and different peak wavelengths. Lines from dotted, dash-dotted to solid exemplify the effects of modulation of increasing amplitude.

issues demanding further investigations when the LSP is sitting close to the interband transitions of the metal. First of all, contrary to the case of SPPs, exhibiting very sharp plasmonic resonances, LSP resonances are typically spectrally broad<sup>[20,21]</sup> (quality factors < 10), and, as such, are affected by a  $\Delta\epsilon$  not only at the resonance peak, but also on a much broader spectrum, where the nonlinear permittivity is highly dispersed. Furthermore, the imaginary component of the optical nonlinearity needs to be taken into account as well, because close to the interband transition it is typically of the same order of magnitude as the real part.<sup>[12,16]</sup>

Here we report on a detailed analysis of the transient optical response of Au nanocrystals with LSP (at 535 nm) near the metal interband transition. Our approach, relying on a combination of ultrafast broadband transient absorption spectroscopy and semi-classical modeling of the energy relaxation processes following photoexcitation, provides a clear-cut picture of the photoinduced dynamics of the plasmonic system. Specifically, disentangling all the different contributions to the transient plasmonic response provides insight into the mechanisms presiding over the experimentally observed negative derivative shape of the dynamic plasmonic spectra. Our results indicate that this shape does not correspond to a mere blue shift of the resonance, but rather stems from a more complex interplay of spectral contributions arising from modulation of both the real and the imaginary parts of Au permittivity induced by the photogenerated hot electrons.

## 2. Results and Discussion

Ultra-clean Au nanostructures were produced with a water-cooled gas aggregation magnetron sputtering cluster source<sup>[22]</sup> (NC200U-B, Oxford Applied Research Ltd.) in DC mode with a power of 29 W, Ar flow of 15 sccm, and aggregation distance of 60 mm. The Au target had a purity of 99.99%. The background and operation pressure were  $1.7 \times 10^{-8}$  and  $1.8 \times 10^{-3}$  mbar, respectively, at room temperature. The metallic particles were deposited on fused silica substrates with a particle density of about 30 nanoparticles/ $\mu\text{m}^2$  as obtained by atomic force microscopy (AFM), and according to the transmission electron microscopy (TEM) images (see Figure S1, Supporting Information), they had an average diameter of  $26.3 \pm 2$  nm (this uncertainty being the standard deviation of the lognormal function fitting the experimental size distribution). As a consequence of the size distribution of the nano-objects, the LSP resonance energy of the sample varies slightly, resulting in a broader absorption band. Deposition of the Au nanoparticles on a-C TEM grids provided detailed information about their structure by TEM, performed with a Philips CM10 TEM (FEI) with an accelerating voltage of 80 kV. Images show a very high degree of crystallinity for the nanostructures, as observed from the clear presence of facets due to crystal planes in **Figure 2a**, thus implying deviations from a spherical shape. This effect, combined with size dispersion of the nanoparticles, is expected to further broaden the static LSP resonance. However, in agreement with previous reports,<sup>[23]</sup> such a high degree of crystallinity has no significant impact on the dynamical response we investigated.

The static absorbance of the sample  $A(\lambda) = -\log_{10}[T(\lambda)]$ , being  $T(\lambda)$  the static transmission spectrum at normal incidence,

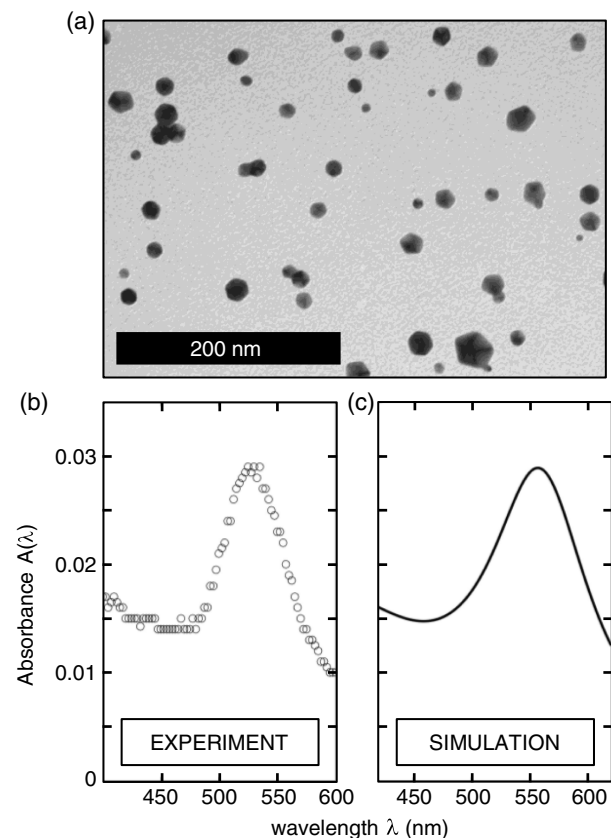


**Figure 2.** a) Transmission electron microscope (TEM) image of the sample, made of Au highly crystalline nanoparticles. b,c) Experimental b) and simulated c) static absorbance spectrum of the sample, showing a well-defined plasmonic peak around 535 nm.

is shown in Figure 2b,<sup>[24]</sup> exhibiting a well-defined resonant peak at 535 nm. The experimental static spectrum is compared to simulated absorbance, which has been obtained by resorting to a reduced modeling of the sample based on the quasi-static polarizability of a nanosphere with 24 nm diameter, with Au permittivity from Drude-Lorentz formulas fitted on experimental data<sup>[25]</sup> (see Section S1, Supporting Information, for further details). To mimic the resonance red-shift induced by the substrate and the high degree of crystallinity (see, e.g., refs. [26,27]), the refractive index of the environment,  $n_{\text{env}}$ , was taken as a fitting parameter. Also, by following the approach reported in ref. [28] the inhomogeneous broadening of the plasmonic response due to the relatively broad distribution of sizes was reproduced by increasing the Drude damping parameter  $\Gamma$  of the metal permittivity with respect to its bulk value  $\Gamma_0 = 72$  meV.<sup>[28]</sup> The result of our calculations for  $n_{\text{env}} = 1.72$  and  $\Gamma/\Gamma_0 = 6$  are shown in Figure 2c. Note that, compared to the experiment, the simulated absorbance shows a slight red shift of about 15 nm in the plasmon resonance peak. This is mostly attributed to the assumption that a single nanoparticle of average size is used in the model to mimic the extinction from nanoparticles with a size distribution. In fact, beyond the quasi-static approximation, the LSP energy decreases when the size increases, and vice versa. Hence, the extinction peak of an ensemble of plasmonic nanoparticles with

different sizes is red- or blue-shifted compared to the extinction of a monodispersed ensemble with the same average size, depending on the actual size distribution.<sup>[29]</sup> Apart from this, our model is capable of reproducing not only qualitatively, but also quantitatively the static absorbance of the sample. Additionally, this discrepancy has no substantial impact on the physical mechanisms under investigation, as it simply translates into a slight red shift of the transient optical spectra, as shown in the following.

To investigate the dynamical response of the sample on an ultrafast timescale, transient absorption spectroscopy was employed. In particular, the samples were excited by 100 fs laser pulses (pump) centered around  $\approx 3.1$  eV (400 nm), obtained by second harmonic generation of the output of a regeneratively amplified Ti:sapphire laser system, and reaching a maximum fluence of  $5 \text{ mJ cm}^{-2}$ . After the photoexcitation, the dynamical evolution of the system was monitored by the differential transmittance of a delayed broadband pulse (probe), namely by measuring the variation of the probe transmission with respect to the equilibrium ( $\Delta T/T$ ), at different pump-probe delays. The white-light continuum probe pulses were generated by focusing the fundamental of the laser on a 2 mm thick sapphire plate and covering the spectral range between 1.7 and 3.5 eV (that is, 350–730 nm). Further details are provided in Section S2, Supporting Information.

Figure 3a shows a map of the measured  $\Delta T/T$  as a function of the pump-probe delay and the probe wavelength in the visible spectral range (450–600 nm). For an excitation fluence of  $0.4 \text{ mJ cm}^{-2}$  a pronounced  $\Delta T/T$  signal exceeding  $\pm 1\%$  is recorded, with a positive band peaked at around 550 nm and a negative band with a peak at 480 nm. Since the optical transmission can be expressed as  $T = 1 - E$ , with  $E$  the extinction of the sample (due to absorption and scattering mechanisms), the positive wing of the  $\Delta T/T$  map corresponds to a spectral region where the transient extinction is decreased compared to the static value, and, vice versa, the negative  $\Delta T/T$  signal corresponds to an increase of extinction. In agreement with the sketch of Figure 1b, a negative derivative shape (corresponding to a blue

shift) for the extinction spectrum is indeed observed. To analyze the shape of the measured  $\Delta T/T$  spectra and rationalize its negative derivative character, we fitted the map cross-section recorded at the 1 ps time delay (solid curve in Figure 3b) with a double-Gaussian spectrum, following the rationale discussed in Figure 1. More precisely, for  $\Delta T/T = T_2/T_1 - 1$ , with  $T_{1,2} = 1 - E_{1,2}$  the transmittance of the sample under static or dynamic conditions, respectively, we considered the corresponding static  $E_1$  and dynamic  $E_2$  extinctions as given by the following formula

$$E_{1,2} = E_b + A_{1,2} \exp \left[ -\frac{(\lambda - \lambda_{1,2})^2}{2w^2} \right] \quad (1)$$

In the equation,  $E_b$  is the non-resonant background extinction, while  $A_{1,2}$  and  $\lambda_{1,2}$  are, respectively, the amplitudes (of opposite sign) and peak positions of the Gaussian resonant spectra, of width  $w$ , to be fitted (with subscript 1 (2) referring to the static (excited) plasmonic resonance). The Gaussian spectrum is taken as an approximation for the Voigt lineshape which is the convolution of the plasmon resonance (which has a Lorentzian lineshape<sup>[30]</sup>) and the gold nanoparticle size distribution, which strongly approaches a Gaussian distribution.<sup>[24]</sup> Results of the fitting procedure (dash-dotted curve in Figure 3b) are in excellent agreement with the experimental spectral trace. To study the effects of increasing excitation levels on the  $\Delta T/T$  spectra, the pump pulse fluence was varied between 0.18 and  $3.4 \text{ mJ cm}^{-2}$  (the full differential transmittance maps are shown in the Section S2, Supporting Information). The different spectra recorded at 1 ps time delay were then fitted with the double-Gaussian profile, and the set of fitting parameters  $\lambda_1$ ,  $\lambda_2$ ,  $A_1$ ,  $A_2$  and  $E_b$  were collected as a function of the laser fluence.

Note that, in agreement with the general picture of a transient blue shift of the plasmonic resonance,  $\lambda_1 \approx 535$  nm regardless of the pump fluence, whereas  $\lambda_2$  progressively blue-shifts to shorter wavelengths with increasing values of fluence (Figure 4a). However, when inspecting the Gaussian-fit amplitudes  $A_1$  and  $A_2$ , width  $w$  and the background parameter  $E_b$ , it is clear that they strongly depend on the pump fluence, instead of being

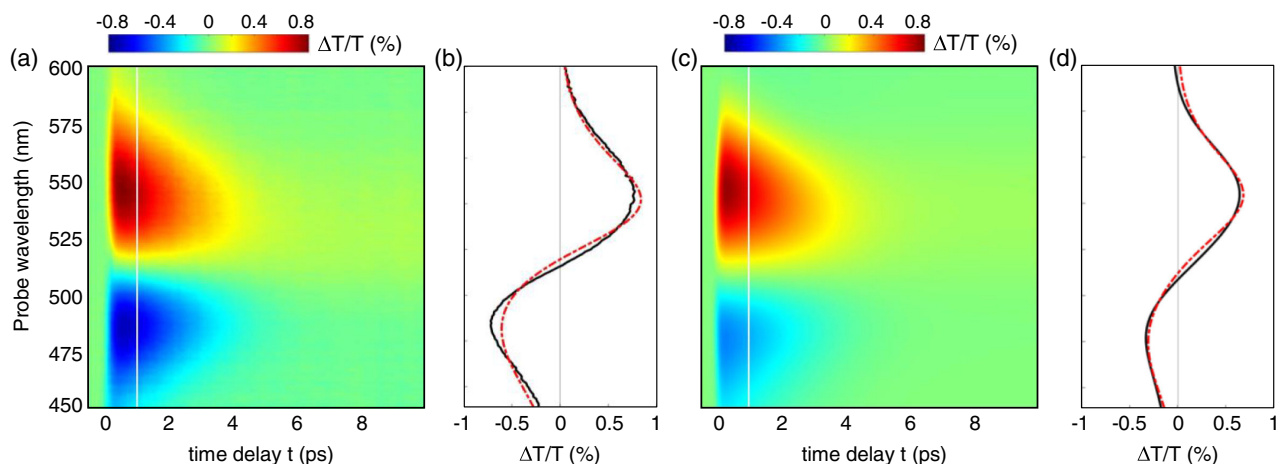


**Figure 3.** a) Measured transient differential transmission map under  $0.4 \text{ mJ cm}^{-2}$  pump laser fluence at 400 nm; b) spectral section of the 2D map evaluated at a time delay of 1 ps (solid line) and Gaussian fit according to Equation (1) (dash-dotted line); c,d) same as (a,b), respectively, for the transient transmittance simulated by the physical model. Vertical white lines in (a) and (b) identify the 1 ps time delay.

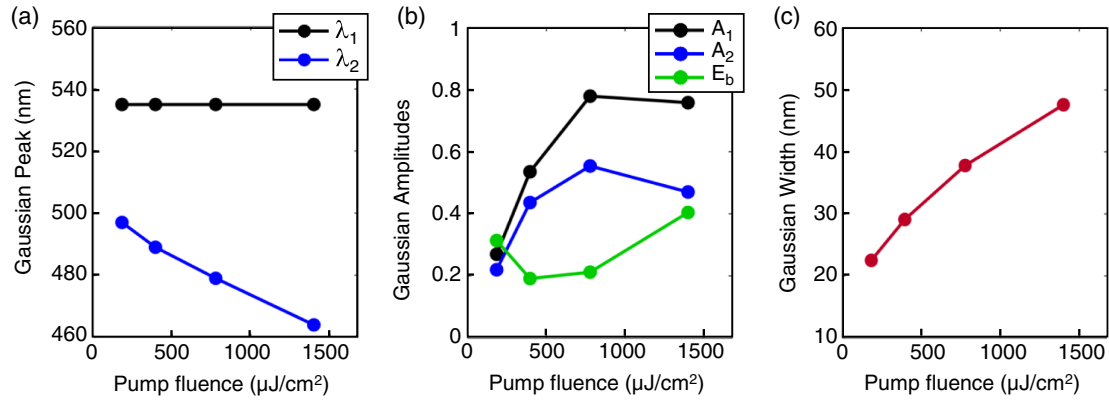


**Figure 4.** a) Peak position  $\lambda_{1,2}$ , b) amplitude  $A_{1,2}$ , and c) width  $w$  of the two Gaussian profiles of Equation (1), retrieved when fitting the differential transmittance signal  $\Delta T/T$  at 1 ps time delay by varying the pump fluence. The fitted background level  $E_b$  (green) is also shown in panel (b).

constant. Moreover, they show a non-monotonic trend, which is opposite for  $E_b$  compared to  $A_1$  and  $A_2$ . This observation is a clear-cut indication that the plasmonic resonance is not experiencing a mere blue shift and suggests that more complex effects than the Fröhlich mechanism outlined in Figure 1a are taking place to accurately account for the negative derivative shape of the photoexcited spectra.

To better understand the nonequilibrium optical response of the plasmonic nanostructures, we performed numerical simulations of the transient absorption spectroscopy experiments by implementing a physical model of the photoexcitation and generation/relaxation of energetic (hot) out-of-equilibrium carriers, based on the so-called three-temperature model (3TM).<sup>[6]</sup> This is a well-established rate-equation model widely employed and validated for metallic<sup>[31]</sup> as well as semiconducting<sup>[32]</sup> nanostructures upon ultrashort laser pulse illumination, for both inter- and intraband excitation conditions (see Section S3, Supporting Information). In this framework, the light–matter interaction between the pump pulse and the plasmonic material and the ensuing ultrafast energy exchanges are described in terms of three internal energetic degrees of freedom: the excess energy stored in a non-thermal fraction of the photoexcited electronic population,  $N$ , the temperature of thermalized electrons  $\Theta_E$ , and the metal lattice temperature  $\Theta_L$ . The model, accounting for the dynamical evolution of these three interlinked energetic variables of the system, reads as follows

$$\frac{dN}{dt} = p_a(t) - aN - bN \quad (2)$$

$$C_E \frac{d\Theta_E}{dt} = aN - G(\Theta_E - \Theta_L) \quad (3)$$

$$C_L \frac{d\Theta_L}{dt} = bN + G(\Theta_E - \Theta_L) \quad (4)$$

In the above-mentioned equations,  $p_a(t)$  is the pump power density absorbed by the plasmonic nanostructure, which excites the non-thermalized electron distribution. Such quantity is written starting from the characteristic parameters of the pump pulse (fluence, time duration, wavelength), together with the system absorption. The (constant) coefficients in the three equations

govern instead the energy relaxation processes triggered by pump absorption. Specifically,  $a$  rules the electron gas heating via electron–electron scattering processes,  $b$  and  $G$  account for the electron–phonon scattering events undergone by non-thermal and thermalized electrons, respectively,  $C_E$  ( $C_L$ ) is the electron (metal lattice) heat capacity. Further details on the definition of these coefficients and values used in the simulations can be found elsewhere.<sup>[31,33]</sup> With the dynamical evolution of the three internal energetic variables of the illuminated system, the photo-induced permittivity modulation corresponding to the excited conditions of the electronic and phononic populations of the system should be determined. To do so, we employed a semiclassical model of the thermo-modulational nonlinearities of Au,<sup>[34]</sup> in which each of the three variables of the 3TM leads to a complex-valued permittivity modulation evolving in time and dispersed over the visible range of wavelengths. The total change in permittivity is then written as the superposition of the three contributions,  $\Delta\epsilon(\lambda, t) = \Delta\epsilon_N(\lambda, t) + \Delta\epsilon_{\Theta_E}(\lambda, t) + \Delta\epsilon_{\Theta_L}(\lambda, t)$ . In brief, both  $N$  and  $\Theta_E$  drive an ultrafast modulation of the Au interband transitions, resulting from the smearing of the electronic energy occupancy distribution. In particular, we included contributions from the transitions close to both the  $L$  and the  $X$  points of the first Brillouin zone of Au in the calculations. This light-driven change modifies the absorption profile of the much weaker probe beam, an intrinsic nonlinear process modeled by varying the imaginary part of the metal permittivity, the corresponding real part modulation being then retrieved by Kramers–Kronig relations. The intraband term of the Au permittivity is instead modified by an increase in  $\Theta_L$ , which modifies the Drude damping factor and the metal plasma frequency. Then, with the dynamical evolution of  $\Delta\epsilon$  at hand, we iteratively applied the same approach used to obtain the static absorbance of the sample in the quasi-static limit (see Section S3, Supporting Information) to determine the transient extinction and corresponding differential transmittance  $\Delta T/T$  signal, at each pump–probe time delay over the broad probe bandwidth.

The results of the numerical simulations are reported in Figure 3, where the calculated map (Figure 3c) and a spectral cut at 1 ps delay (Figure 3d) are directly compared with measurements (Figure 3a,b respectively). Indeed, our physical model

reproduces the measurements in terms of dynamics, intensity, and spectral features of the  $\Delta T/T$  signal with remarkable accuracy. In particular, the negative derivative shape of the transient transmission spectra is observed also in the simulated dynamical signal, exhibiting a transient negative band at shorter wavelengths, from 450 to  $\approx 500$  nm, where the onset of the positive modulation band, extending up to  $\approx 580$  nm, occurs. Moreover, a good agreement between measurements and the results of our physical model is achieved for all the pump fluences employed in the experiments, as detailed in the Supporting Information (compare maps in Figure S2 and S3 and refer to Figure S4, Supporting Information). As for experiments, the fitting procedure applied to the computed  $\Delta T/T$  spectra at a 1 ps time delay succeeds in reproducing the simulated data as a difference between two Gaussian extinction profiles (compare black and red curves in Figure 3d). The same holds for the simulated spectra at increasing fluence, well fitted by Equation (1) at each of the investigated fluences. Specifically, analyzing the outcome of the fitting procedure as with experimental data (Figure 4) leads to comparable results (refer to Figure S5 and Section S3, Supporting Information): all the six fitting parameters depend on the pump fluence, also when numerical spectra are fitted. However, compared to the fit-based approach, our physical 3TM-based model offers the significant advantage of enabling to rationalize the dynamical evolution of the photoexcited system. In particular, it allows us to gain deeper insight into the origin of the observed  $\Delta T/T$  spectra by disentangling contributions arising from different mechanisms and internal energetic variables involved in the photoinduced modulation of the transmission.

First, the complex-valued permittivity modulation  $\Delta\epsilon$  can be analyzed in terms of its three distinct components governed by  $N$ ,  $\Theta_E$ , and  $\Theta_L$  respectively. The corresponding real and imaginary parts of each of these terms can be assessed separately, at each time instant over the broad probe bandwidth. Moreover, to determine how each of the permittivity modulation terms influences the transient differential transmittance (real and imaginary, due to  $N$ ,  $\Theta_E$  and  $\Theta_L$ ), we computed  $\Delta T/T$  as if only one of these contributions at the time was modifying the static permittivity. To the leading order, in the weak perturbation regime (as in the present case, where a moderate pump fluence of  $0.4 \text{ mJ cm}^{-2}$ , well below the damage threshold, was used), the sum of all these disentangled signals thus calculated provides the total  $\Delta T/T$  reported in Figure 3.

The main results of our disentanglement analysis are reported in Figure 5, where 5a–d refer to terms arising from non-thermal hot carriers, Figure 5e–h from thermalised electrons, Figure 5i–l from the metal lattice. By focussing on  $N$  contributions, both the real (Figure 5a) and imaginary (Figure 5d) part of permittivity, evaluated at 100 fs, that is, the time delay when the dynamical evolution of  $N$  reaches its maximum, are negative over the entire visible spectral region. However, a broadband negative  $\Delta\epsilon'$  results in a bisignate dip-peak spectral shape for the ultrafast  $\Delta T/T$ , with the negative band at shorter wavelengths (Figure 5b). Conversely, if only the decrease of  $\Delta\epsilon''$  is considered in the computation, the  $\Delta T/T$  signal is predicted to be negative for all wavelengths (Figure 5c). In contrast, when the metal lattice temperature is considered as the only energetic variable modifying the metal permittivity, both real and imaginary  $\epsilon$  modulation

terms are positive over the entire probe wavelength range (Figure 5i,l, respectively). The effects on the  $\Delta T/T$  are, consistently, opposite compared to the case of non-thermal electrons, namely a broadband increase of  $\Delta\epsilon'$  produces a transmission modulation which is negative (positive) at longer (shorter) wavelengths, and a  $\Delta\epsilon'' > 0$  causes an increase in transmission. Compared to non-thermal electrons, which modify the metal permittivity during the first hundreds of femtoseconds following pump absorption, the modulation arising from the lattice builds up within the first picoseconds, consistently with the typical dynamical evolution, solution of the 3TM.<sup>[31,35]</sup> Likewise, also the spectral features (sign and wavelength-dependence) of the computed permittivity modulations are in agreement with previously reported results.<sup>[33,35]</sup> However, both  $N$  and  $\Theta_L$  are responsible for contributions to the ultrafast  $\Delta T/T$  which are much weaker than the one due to thermalised hot electrons (note the scaling factors in the maps of Figure 5b,c,j,k), which provide the dominant and less trivial contribution to the light-driven modulation. Indeed, the real part of the permittivity changes due to an increase in the electronic temperature (Figure 5e) is highly dispersed over the probe bandwidth, passing from negative to positive values close to  $\approx 530$  nm (again, in agreement with previous reports). Accordingly, the  $\Delta T/T$  signal corresponding to such a  $\Delta\epsilon'$  (Figure 5f) also has a rich spectral structure, with a dominant negative lobe centered around  $\approx 480$  nm, accompanied by weaker positive and again negative modulations at longer wavelengths. Importantly, the observed wavelength dependence of the calculated signal demonstrates that a negative  $\Delta\epsilon'$  (which, moreover, we predict not to remain negative over the entire probe bandwidth) does not suffice to explain the negative derivative character of both the total calculated signal (Figure 3c) and the experimental measurement (Figure 3a). Likewise, the spectrum of  $\Delta\epsilon''$ , in Figure 5h, also changes sign from negative to positive, around  $\approx 480$  nm, that is, where  $\Delta\epsilon'$  is maximum (the two quantities are indeed connected by Kramers–Kronig relations), while it is maximum close to  $\approx 510$  nm. This results in a rather broad positive band in the transient  $\Delta T/T$  calculated as if only  $\Delta\epsilon''$  due to  $\Delta\Theta_E$  contributed to the optical modulation (Figure 5g). Such a positive band at  $\lambda > 500$  nm is indeed the term missing in the purely real calculation (Figure 5f) to match the total one (Figure 3c) and reproduce its negative derivative character. In these terms, the full disentanglement of the ultrafast nonlinear optical response of the structure illustrates the physical origin of the peculiar spectral shape of the transient differential transmittance signal. The bisignate dip-peak  $\Delta T/T$  spectra do not arise from a mere blue shift of the plasmon resonance, corresponding to a decrease in the real part of the metal permittivity. Indeed, the changes in  $\epsilon'$ , mostly (but not exclusively) negative over the visible range of wavelengths, are intrinsically accompanied by modifications of the imaginary part of permittivity. These changes in  $\epsilon''$  also contribute to the ultrafast optical modulation with modifications which are quantitatively comparable to their real counterpart but dispersed in frequency very differently. As such, the interplay between the two contributions, governed by the dynamics of thermalised hot carriers which dominate the optical response of the structure in the conditions analysed, determines the negative derivative shape of the total  $\Delta T/T$ .

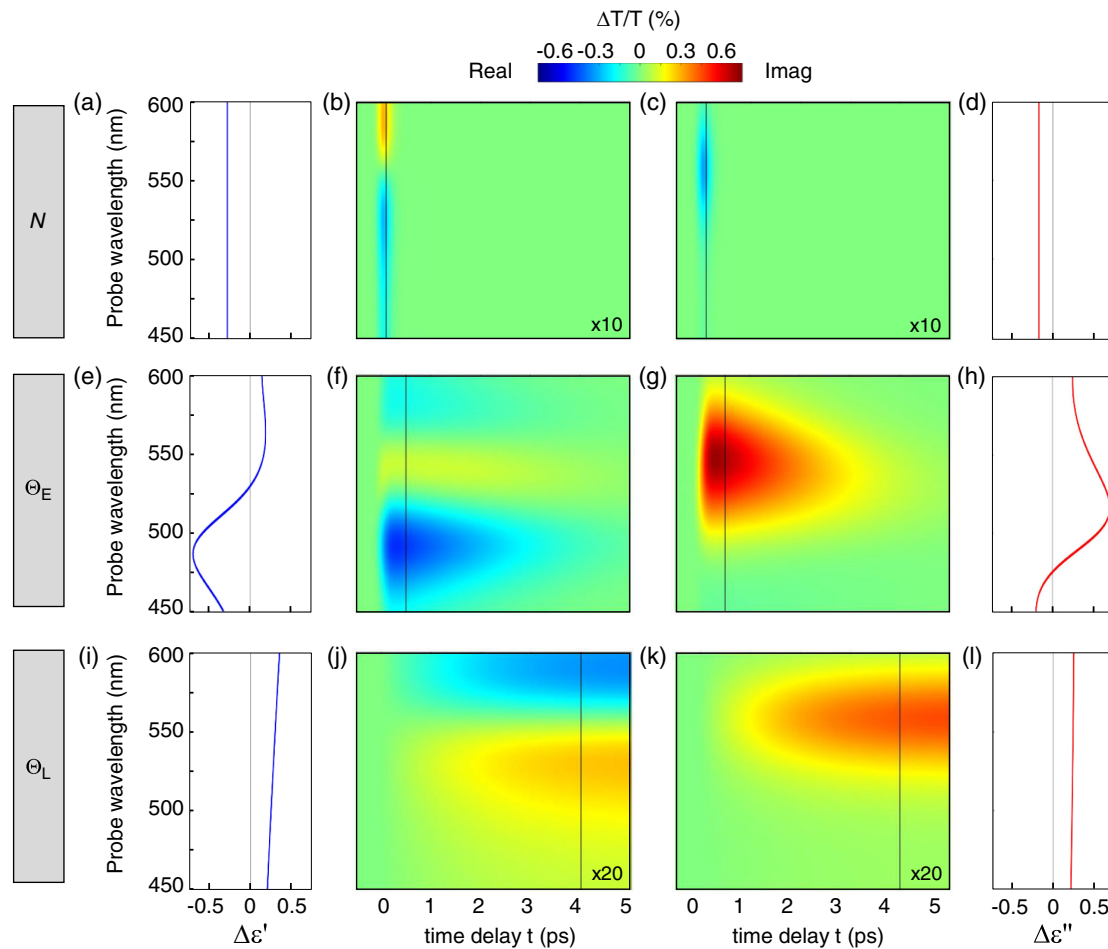


**Figure 5.** Disentanglement of the nonlinear optical response in the ultrafast regime. a–d) Real  $\Delta\epsilon'$  (a) and imaginary  $\Delta\epsilon''$  (d) parts of the complex-valued contribution to permittivity change arising exclusively from nonthermal electrons (described by  $N$ ). Spectra are evaluated at the time delay corresponding to the peak of  $N(t)$ , 100 fs, highlighted by vertical black lines in (b) and (c). The transient optical signal  $\Delta T/T$  is then computed as if only the real (b) or the imaginary (c) components of permittivity were changed by an increase in  $N$ . Maps are magnified by a factor of 10 for better reading. e–h) Same as (a–d) for thermal electrons (described by  $\Theta_E$ ). Permittivity spectra are evaluated at a time delay of 500 fs [peak of  $\Theta_E(t)$ , highlighted by vertical black lines in (f) and (g)]. i–l) Same as (a–d) for metal lattice temperature  $\Theta_L$ . Permittivity spectra are evaluated at 4 ps time delay, highlighted by vertical black lines in (j) and (k). Maps are magnified by a factor of 20 for better reading. Pump fluence was set to  $0.4 \text{ mJ cm}^{-2}$ .

### 3. Conclusion

In this study, we analyzed the ultrafast nonlinear optical response of Au nanocrystals with a plasmon energy close to the onset of the metal interband transitions by means of transient absorption spectroscopy performed at different pump pulse fluences. By applying a reduced model, which fits the differential transmission spectra as a difference between two Gaussian extinction profiles, we demonstrated that a mere blue shift of the Fröhlich resonance, corresponding to a decrease of the real part of the metal permittivity, does not suffice to explain the negative derivative shape of the measured  $\Delta T/T$  spectrum. To gain insight into the mechanisms presiding over the ultrafast modulation of the optical response of the sample, we employed a physical model accounting for the photogeneration and relaxation of out-of-equilibrium electrons, together with the ensuing ultrafast permittivity variations dictated by the thermo-modulational

nonlinearities of Au. Our model allowed us to accurately reproduce the  $\Delta T/T$  measurements as well as to unfold the different contributions to the ultrafast modulations, that we could ascribe separately to the different mechanisms involved in the photoexcitation. In particular, by disentangling the complex-valued modulation effects due to non-thermal electrons, thermalized hot carriers, and the metal lattice respectively, we provided a detailed explanation of the negative derivative shape of the transient  $\Delta T/T$  spectra. Conversely, the results of our disentanglement analysis elucidate that the observed behavior in the transient pump–probe signal should be rationalized as the result of an intrinsic interplay of both the real and the imaginary components of the optical modulation arising from the photoexcited hot carriers. By a comprehensive disentanglement of the ultrafast nonlinear optical response of metallic nanoparticles, we identified the fundamental mechanisms presiding over the photoinduced transient behavior of plasmonic resonances close to the

material interband transitions, shedding light on the origin of the characteristic and often misinterpreted spectral shape of the ultrafast differential extinction of such systems.

## Supporting Information

Supporting Information is available from the Wiley Online Library or from the author.

## Acknowledgements

G.D.V. and M.D.V. contributed equally to this work. This publication is part of the METAFast project that received funding from the European Union Horizon 2020 Research and Innovation Programme under Grant Agreement No.899673. This work reflects only the authors' view and the European Commission is not responsible for any use that may be made of the information it contains. M.D.V. acknowledges assistance from Alessandro Podesta and Jonathan Cardoso with AFM, Maura Francolini with TEM, and Sarita Marom and Ritika Modi with sample preparation. M.G.S, D.C.T-F, and A.M.d.P. acknowledge financial support from the Brazilian funding agencies Capes, Fapemig and CNPq.

## Conflict of Interest

The authors declare no conflict of interest.

## Data Availability Statement

The data that support the findings of this study are available from the corresponding author upon reasonable request.

## Keywords

nonlinear plasmonics, plasmonic nanoparticles, ultrafast spectroscopy

Received: March 21, 2022

Revised: June 24, 2022

Published online:

- [1] M. L. Brongersma, N. J. Halas, P. Nordlander, *Nat. Nanotechnol.* **2015**, *10*, 25.
- [2] J. G. Liu, H. Zhang, S. Link, P. Nordlander, *ACS Photonics* **2017**, *5*, 2584.
- [3] X. Wang, Y. Guillet, P. R. Selvakannan, H. Remita, B. Palpant, *J. Phys. Chem. C* **2015**, *119*, 7416.
- [4] G. Della Valle, M. Conforti, S. Longhi, G. Cerullo, D. Brida, *Phys. Rev. B* **2012**, *86* 155139.
- [5] H. Baida, D. Mongin, D. Christofilos, G. Bachelier, A. Crut, P. Maioli, N. Del Fatti, F. Vallée, *Phys. Rev. Lett.* **2011**, *107* 057402.
- [6] C.-K. Sun, F. Vallée, L. H. Acioli, E. P. Ippen, J. G. Fujimoto, *Phys. Rev. B* **1994**, *50*, 15337.
- [7] K. F. MacDonald, Z. L. Sámson, M. I. Stockman, N. I. Zheludev, *Nat. Photonics* **2008**, *3*, 55.
- [8] P. Vasa, C. Ropers, R. Pomraenke, C. Lienau, *Laser Photonics Rev.* **2009**, *3*, 483.
- [9] M. Kauranen, A. V. Zayats, *Nat. Photonics* **2012**, *6*, 737.
- [10] G. Della Valle, B. Hopkins, L. Ganzer, T. Stoll, M. Rahmani, S. Longhi, Y. S. Kivshar, C. De Angelis, D. N. Neshev, G. Cerullo, *ACS Photonics* **2017**, *4*, 2129.
- [11] M. R. Shcherbakov, S. Liu, V. V. Zubyuk, A. Vaskin, P. P. Vabishchevich, G. Keeler, T. Pertsch, T. V. Dolgova, I. Staude, I. Brener, A. A. Fedyanin, *Nat. Commun.* **2017**, *8*, 1.
- [12] A. M. Brown, R. Sundararaman, P. Narang, W. A. Goddard, H. A. Atwater, *Phys. Rev. B* **2016**, *94* 075120.
- [13] A. M. Brown, R. Sundararaman, P. Narang, A. M. Schwartzberg, W. A. Goddard III, H. A. Atwater, *Phys. Rev. Lett.* **2017**, *118*, 087401.
- [14] L. V. Besteiro, X.-T. Kong, Z. Wang, G. Hartland, A. O. Govorov, *ACS Photonics* **2017**, *4*, 2759.
- [15] N. Del Fatti, F. Vallée, C. Flytzanis, Y. Hamanaka, A. Nakamura, *Chem. Phys.* **2000**, *251*, 215.
- [16] M. Conforti, G. Della Valle, *Phys. Rev. B* **2012**, *85* 245423.
- [17] N. Rotenberg, J. N. Caspers, H. M. van Driel, *Phys. Rev. B* **2009**, *80* 245420.
- [18] S. A. Maier, *Plasmonics: Fundamentals and Applications*, Springer Science & Business Media, New York **2007**.
- [19] M. G. Silva, D. C. Teles-Ferreira, L. Siman, C. R. Chaves, L. O. Ladeira, S. Longhi, G. Cerullo, C. Manzoni, A. M. de Paula, G. Della Valle, *Phys. Rev. B* **2018**, *98*, 115407.
- [20] S. Link, M. A. El-Sayed, *Int. Rev. Phys. Chem.* **2000**, *19*, 409.
- [21] F. Wang, Y. R. Shen, *Phys. Rev. Lett.* **2006**, *97*, 20.
- [22] H. Haberland, M. Mall, M. Moseler, Y. Qiang, T. Reinert, Y. Thurner, *J. Vac. Sci. Technol., A* **1994**, *12*, 2925.
- [23] N. Goubet, I. Tempra, J. Yang, G. Soavi, D. Polli, G. Cerullo, M. P. Pileni, *Nanoscale* **2015**, *7*, 3237.
- [24] G. Faraone, R. Modi, S. Marom, A. Podestá, M. Di Vece, *Opt. Mater.* **2018**, *75* 204.
- [25] P. G. Etchegoin, E. C. L. Ru, M. Meyer, *J. Chem. Phys.* **2006**, *125*, 164705.
- [26] A. Sánchez-Iglesias, I. Pastoriza-Santos, J. Pérez-Juste, B. Rodríguez-González, F. García de Abajo, L. Liz-Marzán, *Adv. Mater.* **2006**, *18*, 2529.
- [27] A. A. Ashkarran, A. Bayat, *Int. Nano Lett.* **2013**, *3*, 50.
- [28] M. Husnik, S. Linden, R. Diehl, J. Niegemann, K. Busch, M. Wegener, *Phys. Rev. Lett.* **2012**, *109* 233902.
- [29] G. Della Valle, D. Polli, P. Biagioni, C. Martella, M. Giordano, M. Finazzi, S. Longhi, L. Duo, G. Cerullo, F. B. De Mongeot, *Phys. Rev. B* **2015**, *91*, 235440.
- [30] X. Fan, W. Zheng, D. J. Singh, *Light Sci. Appl.* **2014**, *3*, e179.
- [31] M. Zavelani-Rossi, D. Polli, S. Kochtcheev, A.-L. Baudrion, J. Béal, V. Kumar, E. Molotokaite, M. Marangoni, S. Longhi, G. Cerullo, P.-M. Adam, G. Della Valle, *ACS Photonics* **2015**, *2*, 521.
- [32] R. Gaspari, G. Della Valle, S. Ghosh, I. Kriegel, F. Scotognella, A. Cavalli, L. Manna, *Nano Lett.* **2017**, *17*, 7691.
- [33] A. Schirato, M. Maiuri, A. Toma, S. Fugattini, R. Proietti Zaccaria, P. Laporta, P. Nordlander, G. Cerullo, A. Alabastri, G. Della Valle, *Nat. Photonics* **2020**, *14*, 723.
- [34] R. Rosei, *Phys. Rev. B* **1974**, *10*, 474.
- [35] S. Dal Conte, M. Conforti, D. Petti, E. Albiseti, S. Longhi, R. Bertacco, C. De Angelis, G. Cerullo, G. Della Valle, *Phys. Rev. B* **2014**, *89*, 125122.